International Conference on Space Optics—ICSO 2022

Dubrovnik, Croatia

3–7 October 2022

Edited by Kyriaki Minoglou, Nikos Karafolas, and Bruno Cugny,

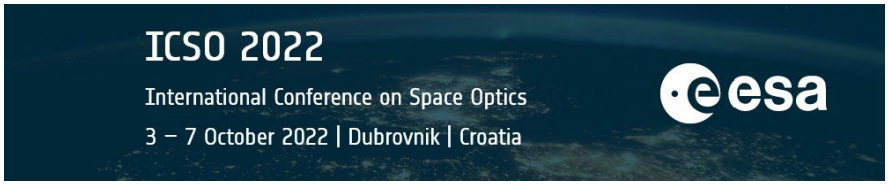

Pre-flight Calibration and Characterization of the EnMAP Sensor

International Conference on Space Optics — ICSO 2022, edited by Kyriaki Minoglou, Nikos Karafolas, Bruno Cugny, Proc. of SPIE Vol. 12777, 127774V · © 2023 ESA and CNES · 0277-786X · doi: 10.1117/12.2690893

Pre-flight Calibration and Characterization of the EnMAP Sensor

Simon Baur*[a], Martin Mücke[a], Bernhard Sang[a], Richard Wachter[a], Matthias Lettner[a], Hans-Peter Honold[a] , Manuela Sornig[b], Sebastian Fischer[a]
[a]OHB System AG, Manfred-Fuch-Str. 1, D-82234 Weßling, Germany; [b]German Aerospace Center (DLR), Königswinterer Str. 522-524, D-53227 Bonn, Germany

ABSTRACT

We present the measurement results of the pre-flight characterization and calibration of the EnMAP HyperSpectral Imager (HSI) and draw conclusions on the performance of the instrument itself as well as the optical ground support equipment (OGSE) deployed. The HSI is capable of measuring the solar irradiance reflected from the Earth's surface as a continuous spectrum in the spectral range of 420 nm to 2450 nm, with an average spectral sampling of 6.5nm (VNIR) and 10nm (SWIR). The EnMAP swath of 30 km is sampled with 30 m in along and across track direction.

The on-ground characterization was performed in air comprising a spectral, geometric, radiometric, polarimetric, and stray light characterization. For spectral calibration, a monochromator setup was used to characterize the spectral response function of the instrument yielding a wavelength and spectral resolution calibration including spectral smile. Geometric calibration was performed using a knife edge in the focal plane of a collimator allowing to determine the line of sight of each pixel. Additionally, the keystone and MTF performance of the instrument was confirmed. A large integrating sphere was used for radiometric characterization of the instrument. This provides an on-ground baseline calibration of radiometric coefficients and response non-uniformity to be updated in orbit. Additionally, the noise performance of the instrument was validated. A polarizer was used to measure polarization sensitivity of the instrument which was found to be in excellent agreement with expectations. Finally a stray light characterization of the instrument was conducted.

Keywords: EnMAP, hyperspectral, calibration, spectrometer, remote sensing, earth observation

1. INTRODUCTION

1.1 EnMAP Mission

The Environmental Mapping and Analysis Program (EnMAP) is a German space borne science mission that aims to characterize the Earth's environment on a global scale. The applications range from climate change impacts, the monitoring of large ecological systems, land cover changes, biodiversity processes and natural resources, to geo hazard and risk assessments [1].

The satellite is based on a push-broom type concept and operates in a polar, sun-synchronous, low earth orbit in 652 km height. Crucial for the scientific aims of EnMAP are the short target revisit times requiring an agile satellite pointing up to 30° off-nadir. This allows for revisit times of a maximum of 4 days with a single satellite. The EnMAP swath width of 30 km is sampled in spatial direction with a 30 m ground sampling distance (see Figure 1 for illustration). The data handling capacity is designed in order to allow for individual swath lengths of up to 1000 km and total data of 5000 km per day. The single payload of the satellite is the Hyper Spectral Imager (HSI). It is capable of measuring the solar irradiance reflected from the Earth's surface as a continuous spectrum in the spectral range of 420nm to 2450nm, with a spectral sampling of 6.5nm (VNIR) and 10nm (SWIR).

The satellite was successfully launched on the 1st of April 2022 with a design mission lifetime of 5 years. At the time of writing, in-orbit commissioning of the satellite is on-going.

*simon.baur@ohb.de; phone 49 8153 4002-1234; fax 49 8153 4002-940; www.ohb-system.de

(a)

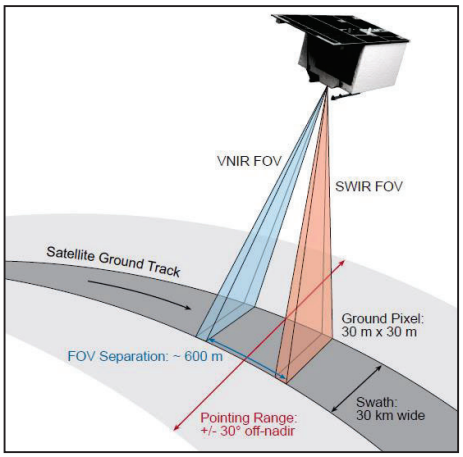

(b)

Mission Requirements	
Altitude	652km
Orbit	Polar, sun synchronous, 11:00 local time
Target revisit time	4 days (30° off nadir)
Pointing accuracy (knowledge)	500m (100m) at sea level
GSD	30m
Swath width	30km
Swath length	up to 1000km

Figure 1 Representation of an EnMAP overpass featuring the dual-spectrometer instrument concept (a). The field-of- views (FOVs) of the visible near-infrared (VNIR) and shortwave infrared (SWIR) spectrometers are separated by ~600m on-ground track and are represented in blue and red, respectively. Selected EnMAP mission requirements are shown in (b)

1.2 Instrument Design

The instrument is designed to cover the spectral range from 420nm to 2450nm, with a spectral sampling of 6.5nm (VNIR) and 10nm (SWIR) at a spectral resolution of < 1.25 SSD. The required SNR is 500 at 495 nm and 150 at 2200 nm. The required radiometric accuracy is 5% with a stability of better than 2.5% over one month. The key design drivers are high optical throughput and low image distortion. A schematic view of the instrument design is shown in Figure 2. The instrument features a nearly diffraction limited three-mirror anastigmatic telescope (TMA) with an across-track field of view (FOV) of ±1.3°. The TMA has an 18 cm entrance aperture and focusses the light from the earth's surface onto a field splitter slit assembly (FSSA). The FSSA includes two separate micro slits for in-field separation of the light and a micro-mirror to redirect the SWIR field into the SWIR spectrometer. Both VNIR and SWIR spectrometer optics have unit magnification. They are derived from an Offner relay imaging concept and employ curved prisms in dual pass configuration as dispersive elements. Light from the spectrometer is finally focused on VNIR and SWIR focal planes arrays that acquire images at a frame rate of 230 Hz with 14-bit resolution. All optical elements are mounted to a monolithic 3-dimensional aluminum structure. To fulfil the stringent requirements on overall pointing stability, the star tracker sensor assembly is directly attached to the optical unit.

In addition to the electro-optical imaging system, the instrument also features a set of calibration devices. A Full Aperture Diffuser Assembly (FADA) at the entrance port allows to switch between earth view, full-aperture sun diffuser calibration and launch protection modes. An on-board calibration sources can be fed into both spectrometers by means of a rotating mirror wheel mechanism. The whole instrument carries dedicated baffling systems ensuring good out-of-field stray light suppression.

In our chosen design, the required geometrical and spectral stability results in stringent requirements on the thermal stability of the instrument's optical unit. Thermal stability is achieved by a heater control combined with an actively controlled, sophisticated loop-heat pipe system.

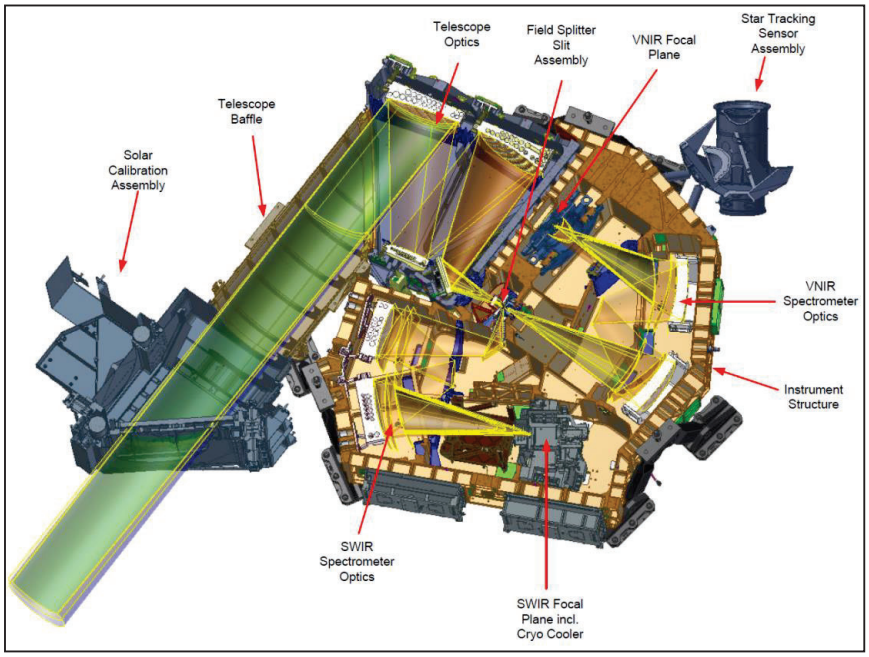

Figure 2 Schematic view of the main components of the EnMAP double-spectrometer instrument concept.

1.3 Calibration Approach

The EnMAP instrument features the capability to validate and update a subset of mission critical calibration tables. The calibration approach is discussed in more detail in [7].

Primary radiometric calibration is achieved using a full-aperture diffuser system (FAD). It carries a Spectralon diffuser with a bidirectional reflectance distribution function that has been characterized with high accuracy on-ground. A mechanism introduces the diffuser into the optical beam in front of the telescope baffle and opens the diffuser protection hatch to allow for direct sun illumination. The validity of the absolute radiometric calibration obtained by sun calibration is monitored using a dedicated on-board calibration assembly (OBCA) on a weekly basis. It consists of a (primary) radiometric integrating sphere, equipped with halogen lamps and blue LEDs to increase the power at short wavelengths. The sphere has an exit port and dedicated projection optics to image the exit port onto the spectrometer entrance slit.

Spectral calibration is performed on a bi-weekly basis in order to ensure the validity of the spectral calibration tables over the mission life time. To this end, a secondary spectral integrating sphere coated with doped diffuser material at its inner surface is connected to the primary sphere. Radiative flux from the spectral sphere is transmitted through the primary sphere to the exit port. The doped material introduces a distinct, stable spectral signature to the output radiance, which is used as a spectral reference for the spectrometer. The spectral signature has been calibrated on-ground in a vacuum chamber and is used together with the on-ground spectral calibration to predict the system performance. Any shift in spectral parameters up to second order can be retrieved by comparing the predicted system performance with on-board measurements.

Detector linearity calibration, pixel response measurements and suspicious pixel mapping will be performed using light-emitting diodes (LEDs) mounted in front of the detectors in conjunction with the ability of the focal planes to control integration time in a wide parameter range. VNIR and SWIR cameras have different LEDs tailored to the quantum efficiencies of the respective detectors. The calibration interval is planned to be one month.

A mechanism is installed in front of the spectrometer slit that is cutting off the optical path from the telescope to the spectrometer. This shutter mechanism is used for regular observational dark reference measurements, typically before and after each earth observation image take. It is further used for switching between the open observation aperture, and the calibration position which is directing the light from the OBCA to the spectrometer entrance slit. To assess the shutter emission, deep space observations are performed together with the shutter measurements during commissioning.

The in-orbit calibration means are complemented by an extensive on-ground calibration campaign the results of which are discussed in more detail in these proceedings.

Absolute radiometric calibration was performed to provide a baseline radiometric calibration and performance validation. Calibration tables generated on ground are to be replaced in-orbit by tables generated from the sun calibration. In addition a characterization of the noise performance of the EnMAP sensor was performed. The results of the radiometric calibrations are discussed in Sec. 4. The radiometric calibration is complemented by a polarimetric characterization which is reported in Sec. 5. A stray light in the instrument was characterized by a dedicated measurement campaign allowing to perform a stray light correction. The results of these measurements will reported in a separate publication.

The in-orbit spectral calibration assembly is capable of accurately detecting global shifts of the spectral calibration and global changes in the spectral smile performance. The on-board spectral calibration method requires an accurate spectral calibration on ground including a characterization of spectral resolution. Measurement results are reported in Sec. 2.

Absolute pointing calibration is performed during in-orbit commissioning using ground control points. However, an accurate relative geometric calibration is required to derive the line of sight for all pixels which is discussed in Sec. 3.

Finally, we conclude with a summary in Sec. 6 drawing the main conclusions from the C&C campaign.

2. SPECTRAL CALIBRATION

2.1 Spectral Response Function

Spectral calibration was performed by applying an optical stimulus to the instrument using a full aperture collimator and recording the instrument response. The calibration was performed at five field positions. For each field position, a spectral scan was performed covering the full spectral range of the EnMAP instrument. The optical stimulus was generated using a monochromator setup. The full spectral range was split up into several partial scans with different monochromator settings. For each partial scan, all monochromator settings were kept constant except for the grating angle. As a result of this, the bandwidth of the stimulus varied over the scan and was chosen to be < 0.2 SSD. The actual bandwidth per scan step was characterized and accounted for in the data processing. In addition, the radiant flux at the exit of the collimator was characterized and was used for normalizing the data. The step size was adjusted for each partial scan range and varied between 0.5 and 1.0 nm. For each illuminated pixel, the signal was recorded as a function of the stimulus wavelength yielding the spectral response function (SRF). A Gaussian model was fitted to the SRF data to extract the center wavelength and the spatial resolution defined as the full width at half maximum (FWHM). Figure 3 shows examples for the SRF. The data quality is very good and the shape of the SRF is accurately captured. The model fits the data generally very well. Deviations from the Gaussian model are only observed at long wavelengths of the VNIR spectrometer where the SRF is affected by the MTF of VNIR detector.

The characterization was performed in air. The refractive index of the air surrounding the spectrometers' prisms differs from that of vacuum resulting in spectral shift of the wavelength calibration from air to vacuum of 4.79 SSD (VNIR) and 2.68 SSD (SWIR) which must be accounted for when deriving a spectral calibration for vacuum conditions. When going from air to vacuum, the spectrum is shifted on the detector into the direction of the blue end of the spectrum. The exact shift is determined using the in-orbit calibration sources. In order to obtain an accurate spectral calibration, the air pressure was recorded and used for correction of the calibration data.

(a) VNIR

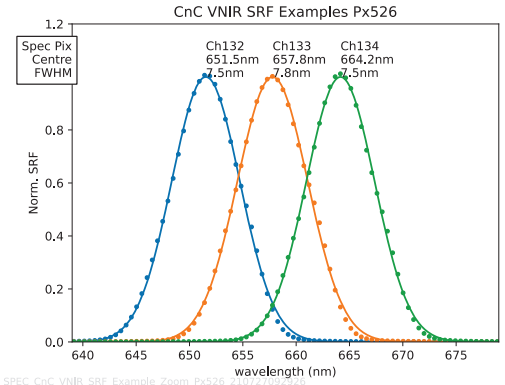

(b) SWIR

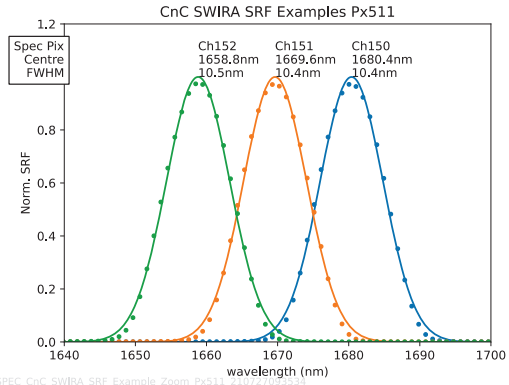

Figure 3 Measured spectral response functions of three adjacent spectral channels are shown for VNIR (a) and SWIR (b). The solid line shows a Gaussian model fitted to the measurement data used to extract center wavelength and the bandwidth.

2.2 Spectral Reference

The center wavelength of the SRF is used to assign a wavelength to each pixel thereby creating a wavelength calibration of the instrument. Figure 4 shows the spectral reference as a function of spectral channel for the five field positions. In these proceedings, the spectral channel index is defined by the detector row index. The dispersion of EnMAP's prism spectrometers is non-linear which is reflected by the non-linear nature of the calibration curve. The air pressure is take into account during the processing of the data. Results are reported for an air pressure of 950 mbar which was the typical air pressure during the measurement campaign. The measurement accuracy (k=2) of the on-ground calibration is estimated to be 0.14 nm and 0.13 nm for VNIR and SWIR, respectively. The measurement accuracy is largely limited by the combined temporal stability of the instrument and the setup. In comparison, the accuracy of the in-orbit spectral calibration is < 0.5 nm (VNIR) and < 1.0 nm (SWIR).

(a) VNIR

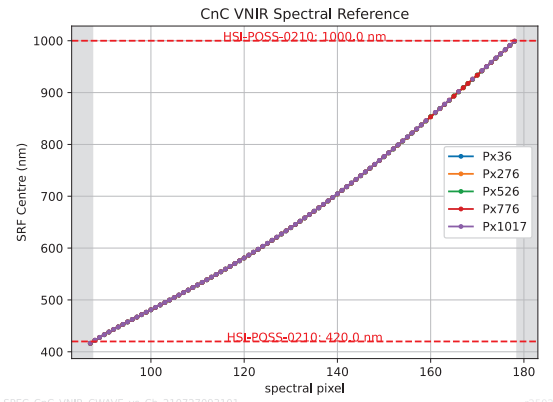

(b) SWIR

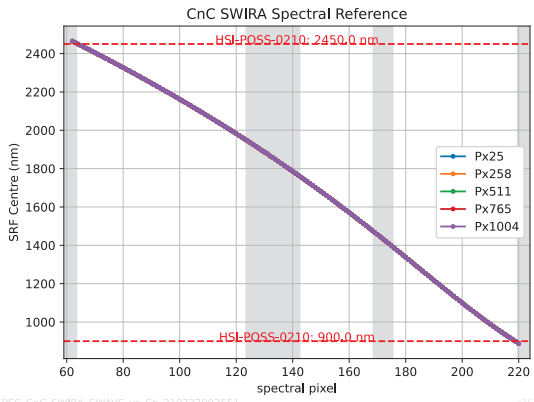

Figure 4 Center wavelength for five detector columns as a function of spectral pixel index for VNIR (a) and SWIR (b). The dispersion of EnMAP's prism spectrometers are non-linear. For the SWIR spectrometer, wavelength decreases with spectral pixel index which is due to the definition of the index. Shaded spectral pixels are not part of the EnMAP spectral ranges and will not be transmitted to ground during earth observation.

2.3 Spectral Sampling Distance

The spectral sampling distance (SSD) is defined as wavelength difference between adjacent spectral channels for a given detector column. It is proportional to the derivative of the curves shown in Figure 4. Figure 5 shows SSD as a function of spectral channel index. The corresponding wavelengths are shown at the top. The spectral sampling distance varies very

little across the field of view. Measurement results are in excellent agreement with predictions from simulations. For VNIR, an etaloning effect in the detector is very apparent which is discussed in more detail in Sec. 2.6.

(a) VNIR

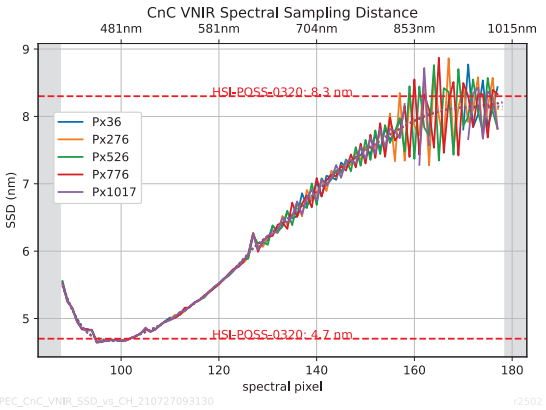

(b) SWIR

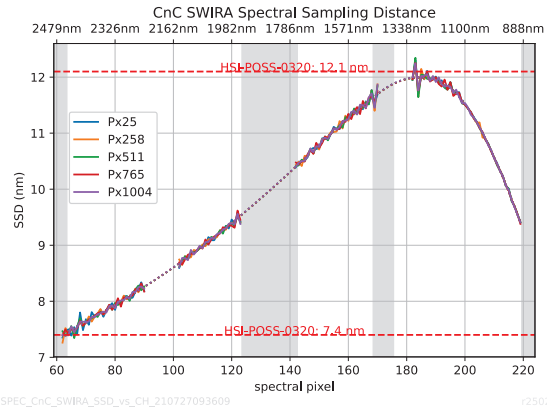

Figure 5 Spectral sampling distance for 5 detector columns as a function of spectral pixel index for VNIR (a) and SWIR (b). The dashed line shows the model fitted to obtain a smooth calibration curve. (a) The jump around pixel index 127 of VNIR coincides with where the two halves of the detector are joined. At long wavelengths, the effect of detector etaloning is clearly visible. (b) The spectral sampling distance is in excellent agreement with expectations. Gaps in the data are due presence of absorption features in air.

2.4 Spectral Smile

Spectral smile describes the wavelength variation of each detector row across the field of view in across-track direction. Figure 6 shows peak-to-valleys variation of the spectral reference for each detector row. For both spectrometers, spectral smile is far below the required 0.2 SSD. For VNIR, spectral smile is dominated by the detector etaloning effect (see Sec. 2.6). Figure 7 shows examples of how the center wavelength varies across the field of view for a selected number of spectral channels. For VNIR, the spectrometer smile is attributed to a very small rotational misalignment of detector to spectrometer resulting in a linear smile signature. For SWIR, smile arises from the prism spectrometer and is in excellent agreement with predictions from simulations. The measurement uncertainty (k=2) is 0.017 SSD and 0.007 SSD for VNIR and SWIR, respectively. It is largely attributed to the combined temporal stability of the setup and the instrument during the measurements.

(a) VNIR

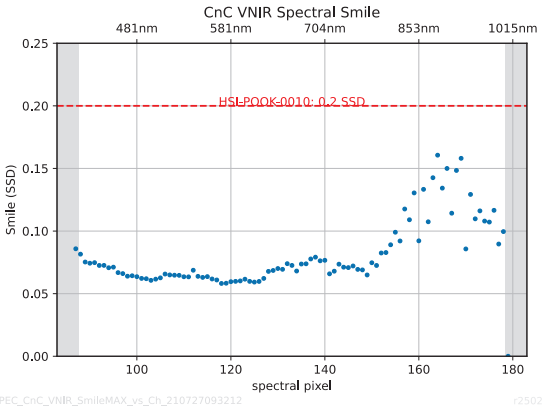

(b) SWIR

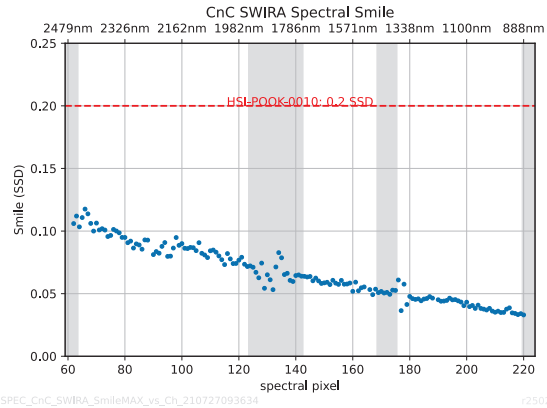

Figure 6 Peak-to-valley spectral smile as a function of spectral channel for VNIR (a) and SWIR (b). For VNIR, spectral smile at long wavelengths is increased due to the detector etalon effects.

(a) VNIR

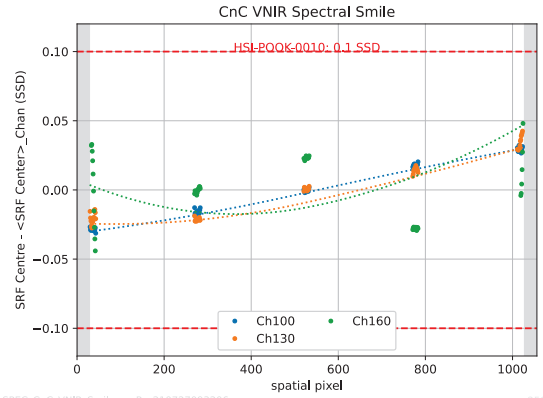

(b) SWIR

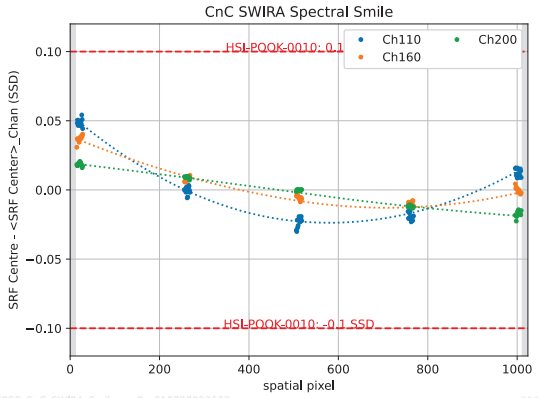

Figure 7 Spectral smile signature for VNIR (a) and SWIR (b) for three spectral channels. For VNIR, the signature is mostly linear superimposed by fringing effects which are not fully resolved in this measurement. For SWIR, the smile signatures changes from linear to parabolic as a function of wavelength.

2.5 Spectral Resolution

Spectral resolution is defined as the FWHM of the Gaussian model fitted to the SRF data. The spectral resolution is dominated by the spectral sampling distance discussed in Sec. 2.3. The spatial resolution reported here has been correct for the finite bandwidth of the optical stimulus which was characterized separately. Corrections are small with < 0.1 nm (VNIR) and < 0.2 nm. Figure 8 shows the spectral resolution for five field positions. For both spectrometers, the spectral resolution varies only very little across the field of view. For VNIR, the detector etaloning is very apparent again and is discussed in more detail in Sec. 2.6. At long wavelengths, the low detector MTF leads to a decrease in spectral resolution. At these wavelengths, deviations from the fit model are noticeable, too. For SWIR, the spectral resolution is in very good agreement with predictions.

(a) VNIR

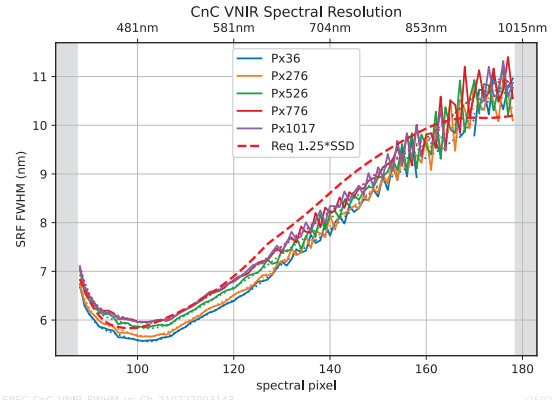

(b) SWIR

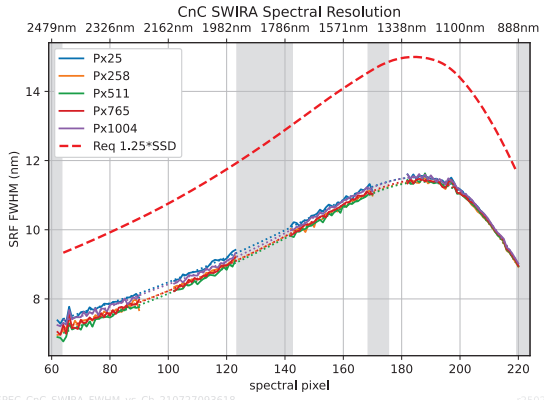

Figure 8 Spectral resolution as a function of spectral channel for five field positions. In VNIR (a) the effect of detector etaloning is clearly visible. The spectral resolution of SWIR (b) is in very good agreement with predictions.

2.6 VNIR Detector Etalon Effect

Optical etaloning in back-illuminated CCD and CMOS devices is a well known effect. Such devices are typically very thin (~10 µm). Reflections between the front and back surface cause them to act as an etalon. This results in unwanted fringing effects. Fringing can be observed in the spatial domain if the thickness of the devices varies and in the spectral domain if the wavelength of the illumination varies. Both types of fringing play a role in EnMAP's VNIR detector. Fringe visibility is only high if losses such as photon to electron conversion are low. For EnMAP's VNIR detector, fringing is visible for

long wavelengths starting from around 600 nm and increasing in contrast towards 1000 nm. At 900 nm, fringe visibility is approximately 0.08. The free spectral range (FSR) of the etalon in the relevant wavelength region is approximately twice the SSD. For EnMAP, fringing has the following consequences:

- Etaloning results in a modulation of the radiometric response of the uncalibrated instrument in across-track direction. This results in an increased response non-uniformity which can be very well corrected by the radiometric calibration. Fringing in the response non-uniformity is shown in Figure 22(a)
- Etaloning results in a modulation of detector QE as a function of wavelength therefore affecting the spectral response function of each pixel and the instrument as a whole. Spectral gradients in the QE effectively lead to a spectral shift of the spectral response function. Because the FSR is approximately 2 SSD, adjacent spectral pixels experience a spectral shift of opposing sign resulting in the very strong modulation signature observed in Figure 5. The actual amplitude of the modulation in the spectral calibration is a factor of ~2 lower. Figure 9(a) shows examples of the fringing for selected spectral channels.
- The curvature of QE as a function of wavelength results in a broadening or narrowing of the spectral response function. For the specific FSR of EnMAP, this results in a modulation of the spatial resolution with a frequency of 1/(2 SSD). Figure 9(b) shows examples of the fringing for selected spectral channels.
- If the spectrum used for radiometric calibration is not completely flat then errors in the spectral calibration due to fringing can induce a spurious signal in the radiometric calibration which must be taken care of. This is accounted for in the radiometric calibration performance budget of EnMAP.

Whilst a change of the fringing pattern is expected ground to orbit due to the air-to-vacuum shift and small changes in detector alignment, the fringing pattern is expected to be stable in orbit due to the excellent temperature stability of the detector. In the spectral region affected by fringing, dedicated measurements were performed with increased number of field positions to resolve the fringes, see Figure 9.

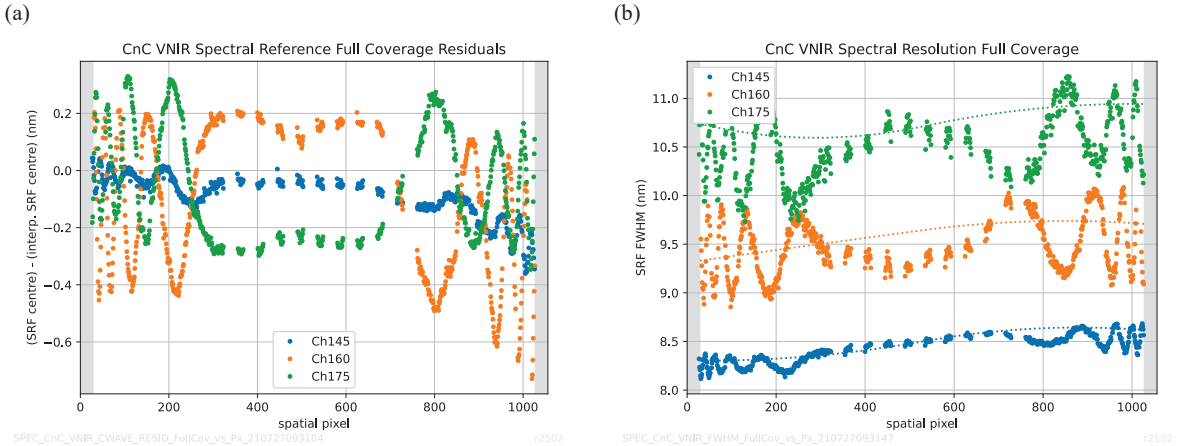

Figure 9 Fringing in the spectral reference (a) and spectral resolution (b) as a function of across-track pixel for selected spectral channels. A dedicated measurement was performed to resolve the structure of the fringing. The etalon thickness has a bath tub structure with near constant thickness at the center and increasing thickness towards the edges resulting in fringes due to changing of the etalon thickness.

3. GEOMETRIC CALIBRATION

3.1 Line Spread Function

Geometric calibration was performed by placing a knife edge in the focal plane of the same collimator that was used for the spectral calibration. Instead of using the spectrally narrow monochromator, a spectrally broad light source (QTH lamp) was used allowing to illuminate many spectral channels of the instrument at once. The collimator together with the instrument optics image the knife edge onto the instrument detectors. Scanning the knife edge perpendicular to the optical axis of the collimator and recording the pixel signals allows to measure the edge spread function. The derivative of the

edge spread function yields the line spread function (LSF). Examples of line spread function are shown in Figure 10 and Figure 11 in across-track and along-track direction, respectively. Scans were performed with a step size of 0.1 px typically covering a range of > 10 GSD. The knife edge position can be related to an angle of an optical alignment cube mounted at the entrance of the instrument telescope. This allows to express the LSF as a function of field angle in a known coordinate system which is defined by a mechanical feature. The optical alignment cube can be related to measurement coordinate system of the star tracker sensors of the attitude control system. Measurements were performed at a minimum of five field positions.

A model is fitted to the measured LSF to extract the line of sight (center of the LSF) and the geometric bandwidth (FWHM of LSF) of each measured pixel. A top hat function convoluted with a Gaussian function is used as the model for fitting. In addition, the Modulation Transfer Function (MTF) can be determined by numerically calculating the Fourier transform of the LSF data.

(a) VNIR (b) SWIR

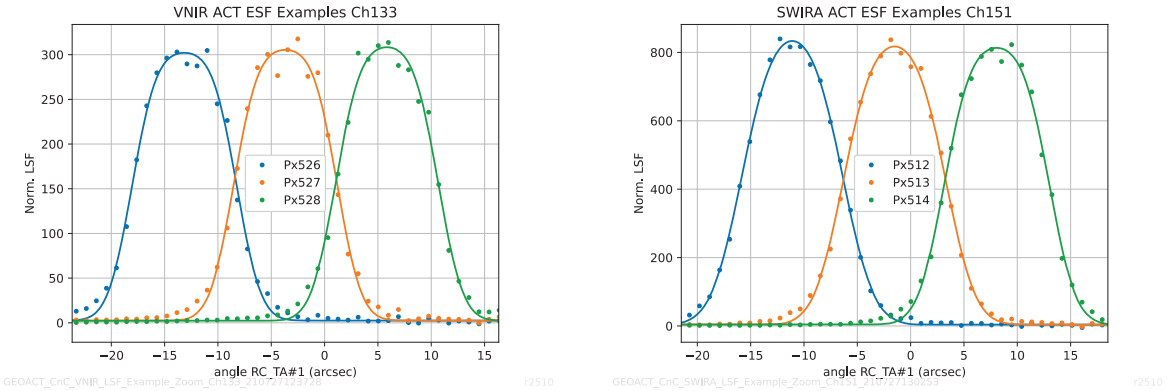

Figure 10 Line spread functions of three adjacent spatial pixels in across-track direction for VNIR (a) and SWIR (b). In across-track direction, the MTF of the telescope and the spectrometer result in noticeable smoothing of the line spread function which otherwise would be of a top hat shape. The solid lines show the fitted models.

(a) VNIR (b) SWIR

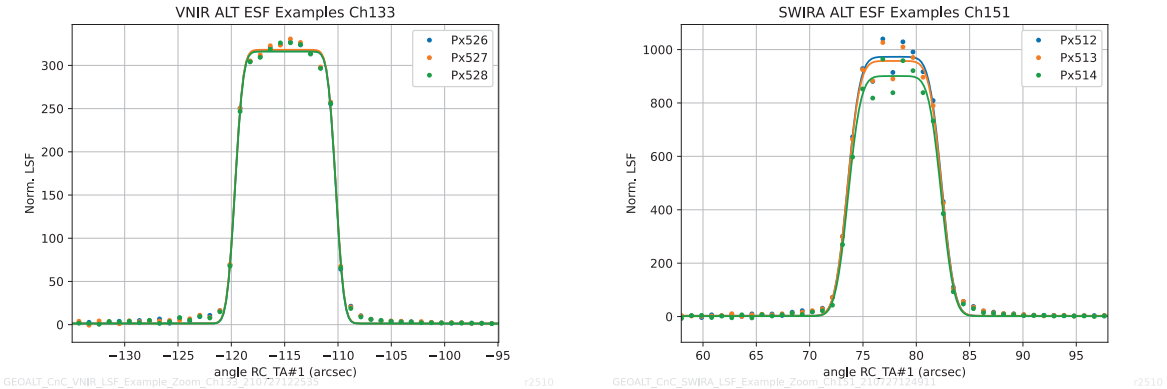

Figure 11 Line spread functions of three adjacent spatial pixels in along-track direction for VNIR (a) and SWIR (b). In along-track direction, only the telescope MTF results in a smoothing of the line spread function. The spectrometers only act as wavelength resolving detectors. Consequently, the LSF resembles much more a top hat function in along-track than in across-track. The solid lines show the fitted models.

3.2 Line of Sight

Figure 12 shows the across-track line of sight as a function of spatial pixel. The difference in line of sight between neighboring pixels gives the angular sampling distance (equivalent to the across-track ground sampling distance) and is on average 9.47228 arcsec. The measured angular sampling distance deviates < 1% from the average. Figure 13 shows the deviation from a bivariate first order polynomial model fitted to the data which is used as the calibration product. The deviation from this fit model < 1.2 arcsec. The spectral terms of the model describe linear keystone which can be used for Keystone correction. The measurement uncertainty (k=2) of the individual pixels' line of sight is estimated to be less than 0.57 arcsec. The residuals shown in Figure 13 are most likely due to optical distortion of the instrument rather than the measurement setup. The measurement uncertainty of all pixels belonging to the same detector column relative to each other is lower, see Sec. 3.3.

(a) VNIR

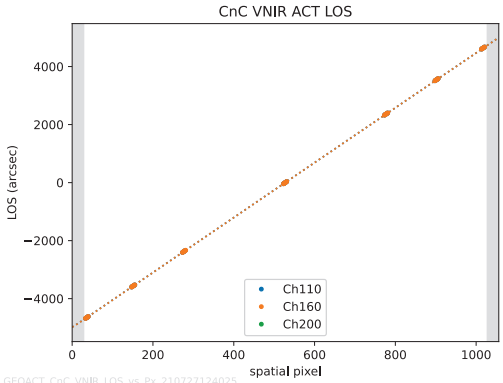

(b) SWIR

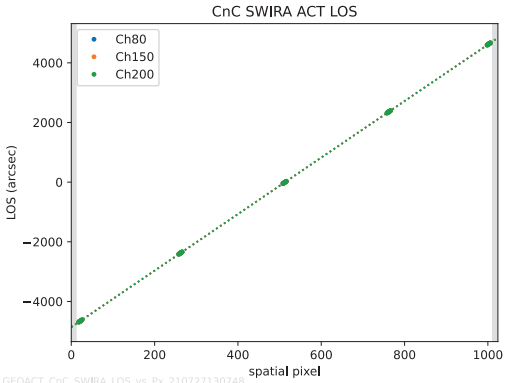

Figure 12 Across-track line of sight as a function of across-track pixel for three spectral channels for VNIR (a) and SWIR (b). The dashed lines show bivariate linear fit model.

(a) VNIR

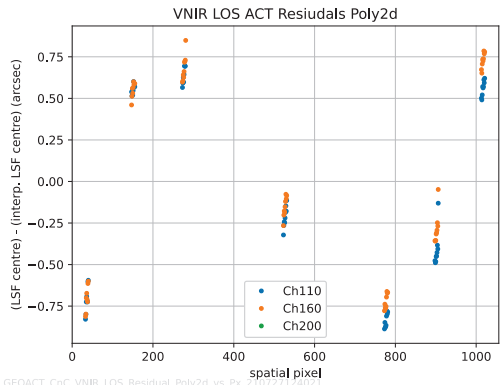

(b) SWIR

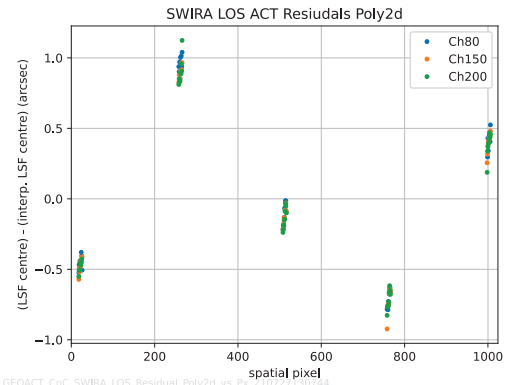

Figure 13 Across-track line of sight fit residuals for three spectral channels. The fit residuals describe the deviation from the bivariate linear fit model. The structure of the fit residuals is similar for VNIR (a) and SWIR (b) wavelength independent. The residuals are reproducible and larger than the estimated measurement uncertainty suggesting that they show the optical distortion of the telescope.

Figure 14 shows the along-track line of sight as a function of across-track pixel. The along-track line of sight varies over the field of view due to the barrel distortion of the telescope. The observed distortion agrees very well with expectations from simulations. Figure 15 shows the same data in a single graph illustrating the field separations of the VNIR and SWIR view. In contrast to across-track LOS, along-track LOS is only affected by the telescope. As expected for a catoptric system, it does not vary with wavelength. A 2nd order polynomial is fitted to the LOS data. The curvature and gradient terms are forced to be the same for both spectrometers considering the very good parallelism of the slits. Despite these

constraints on the fit, the model fits the data very well and fit residuals are < 0.5 arcsec. This is below the measurement uncertainty of 0.57 arcsec (k=2). This measurement uncertainty refers the uncertainty in the line of sight of individual pixels relative to each other. The dataset shown in Figure 15 appears to be rotated around the origin of the coordinate system. This is a measurement artefact and of no practical relevance because it can easily be accounted for in orbit.. Due to the measurement geometry, clocking around the optical axis cannot be accurately determined.

(a) VNIR

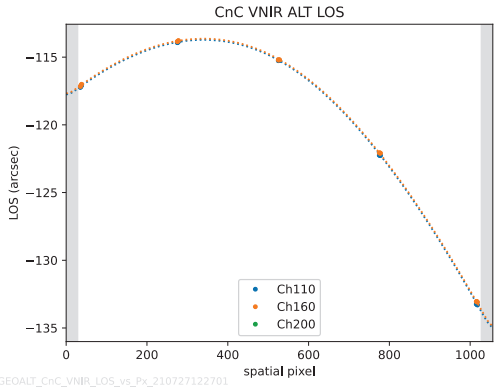

(b) SWIR

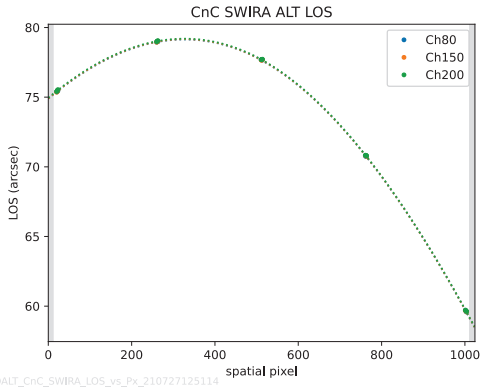

Figure 14 Along-track line of sight for three spectral channels. The dashed lines show 2nd order polynomial fit model which fits the data well.

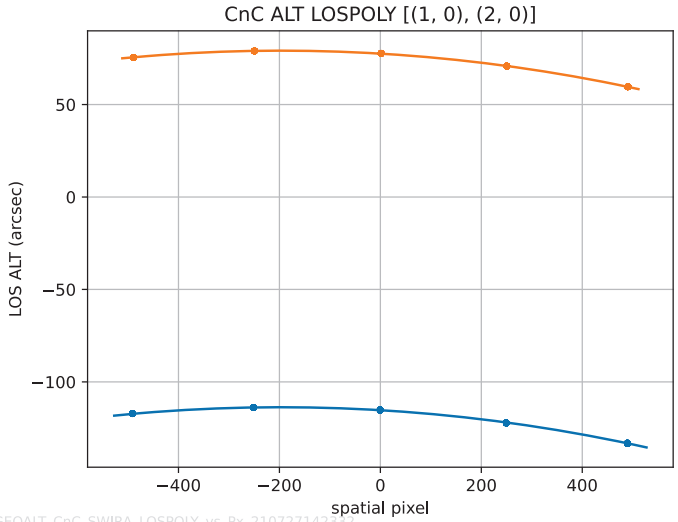

Figure 15 Along-track line of sight as a function of across-track pixel. VNIR (blue) and SWIR (orange) are shown in a common coordinate system defined by the optical alignment cube. The angular offset between the VNIR and SWIR view is owed to the dual slit design of the instrument in which the SWIR view is slightly forward pointing in flight direction compared to VNIR. The field separation is 192.84 arcsec and constant across the field of view despite the barrel distortion.

3.3 Keystone

Spectrometer keystone describes the variation of line of sight with wavelength for a given detector column. Figure 16 shows keystone signatures for five spatial pixels. The observed keystone signatures are very well understood. In particular the keystone of the SWIR spectrometer can very well be described by a linear model and corrected if necessary. Figure 17 summarizes the peak-to-valley keystone values for all spectral channels. The measurement uncertainty (k=2) is 0.076 GSD.

The uncertainty is lower than the uncertainty of the line of sight measurement because the keystone measurement only requires good relative accuracy.

(a) VNIR (b) SWIR

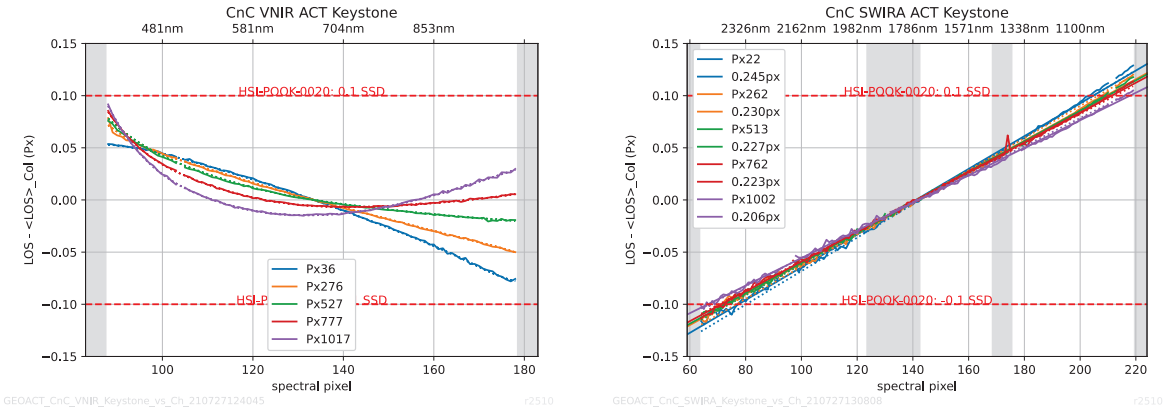

Figure 16 Signatures of spectrometer keystone for five field positions. The SWIR spectrometer (b) shows a linear keystone signature which only slightly varies across the field of view. This signature is attributed to an imperfect alignment of slit and dispersion direction of the spectrometer. The VNIR spectrometer (a) shows the same linear signature superimposed by a more complex structure. The linear slope is the same for both spectrometer if the geometry and difference in pixel sizes is taken into account. The superimposed structure agrees very well with design predictions.

(a) VNIR (b) SWIR

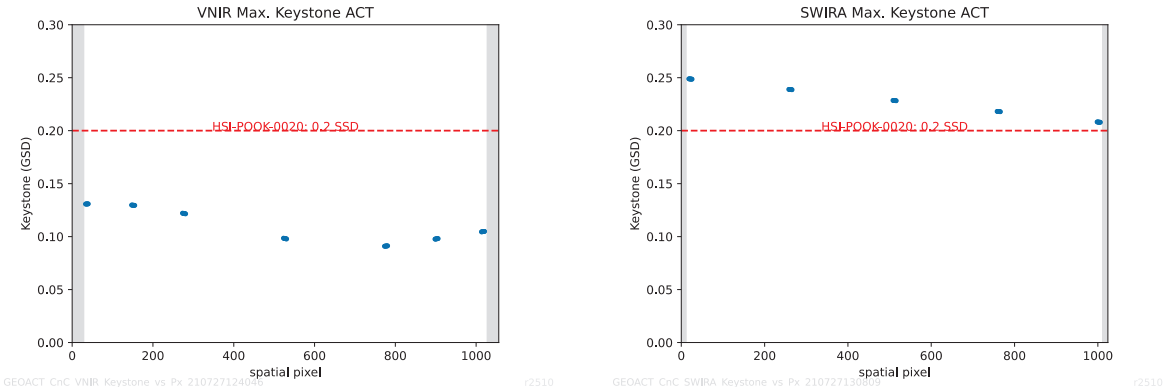

Figure 17 Peak-to-valley keystone as a function of across-track pixel. Keystone is <0.13 and <0.25 GSD for VNIR (a) and SWIR (b) respectively.

3.4 MTF and Spatial Resolution

MTF in along-track direction is high as can be seen from the top-hat like structure of the line spread function shown in Figure 11. This is due to only the telescope contributing to the wave front error which is near diffraction limited.. Figure 18 shows MTF evaluated at the pixel Nyquist frequency 1/(2GSD) as a function of spectral channel with a relative measurement uncertainty (k=2) of < 2.84%. MTF appears to improve towards longer wavelengths which is against the naive expectation for a diffraction limited catoptric system where the optical point spread function increases with wavelength. in diameter This behavior can also be seen more directly in Figure 19 where the FWHM of the line spread function in along-track is shown. It is evident, that the along-track pixel width in object space decreases with wavelength. This behavior can be explained by a diffraction effect at the slit. Diffraction at the slit edge introduces an additional loss channel. Since it affects only light originating from close to the pixel boundary in object space the pixel appears to be

smaller. The range of the effect is determined by the size of the Airy disk that the telescope creates in the plane of the slit for each point source in object space. As the size of the Airy disk increases with wavelength, the range of the effect becomes larger at long wavelength and conversely the effective pixel size in along-track becomes smaller. The effect can be simulated by a simple model with no free fit parameters which agrees very well with the measurement data. At 420nm, the width of the point spread function of the telescope is much smaller than the slit width. Therefore, the effect becomes negligible and data agrees with design predictions. No such wavelength dependence of FWHM of the line spread function can be observed in across-track direction in agreement with the simple model.

(a) VNIR (b) SWIR

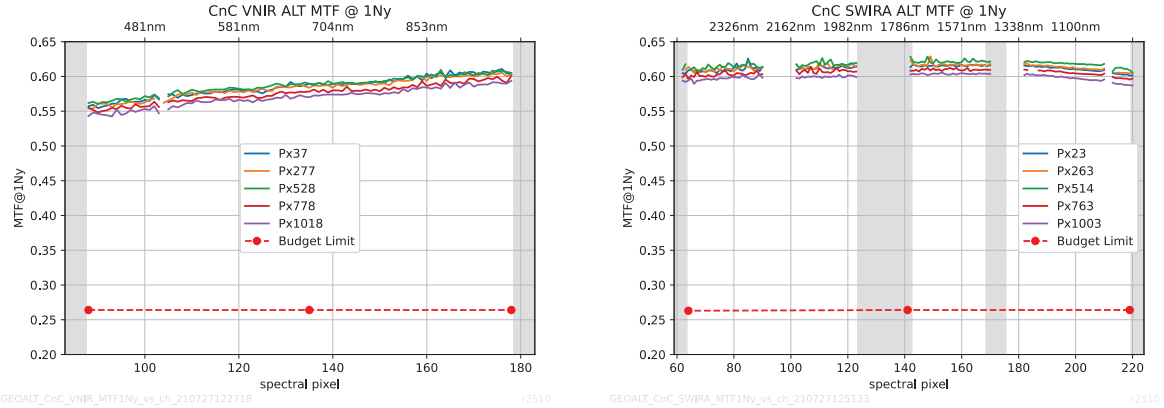

Figure 18 Along-track MTF at the pixel Nyquist frequency as a function of spectral channel for five field points. Against the naïve expectation, MTF increases with wavelength which can be explained by a diffraction effect.

(a) VNIR (b) SWIR

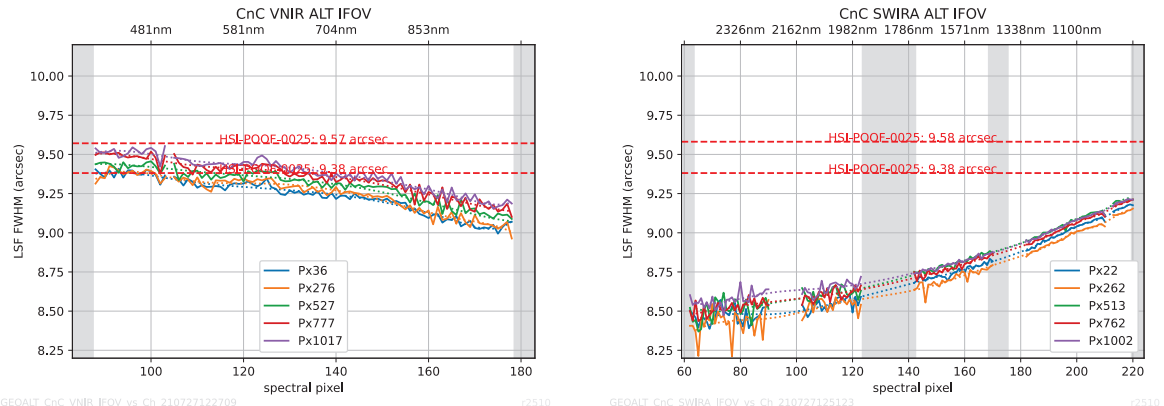

Figure 19 FWHM of the along-track line spread function as a function of spectral channel for five field points. The effective pixel width decreases with wavelength. In the spectral overlap region, results from VNIR (a) and SWIR (b) agree.

MTF in across-track direction is not only affected by the wave front error of the telescope but also by the properties of the spectrometer and the detector resulting in a lower MTF. Figure 20 shows across-track MTF at pixel Nyquist. The relative measurement uncertainty (k=2) is < 3.11%.

(a) VNIR

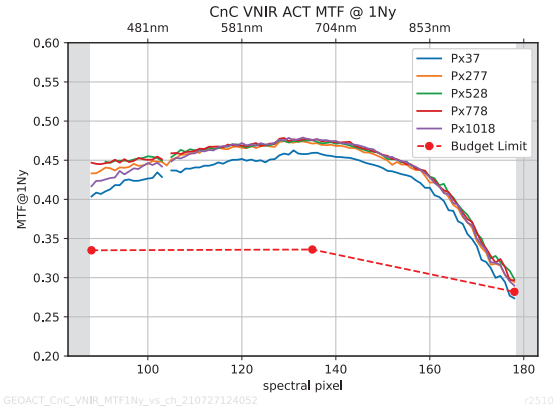

(b) SWIR

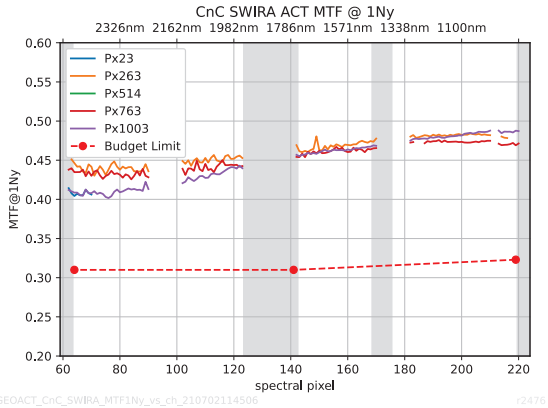

Figure 20 Across-track MTF at pixel Nyquist for five field positions. For VNIR (a), MTF is drops to lower values at long wavelengths. This is due to the wavelength dependence of the detector MTF. The lower MTF value at one extreme of the field can be identified as trifoil wavefront error known from the spectrometer characterization. For SWIR (b) MTF drops only slightly with wavelength.

4. RADIOMETRIC CALIBRATION

4.1 Definitions

The on-ground radiometric calibration serves the purpose of characterizing the instrument performance and providing a baseline calibration. In-orbit radiometric calibration tables are derived using the full aperture sun diffuser.

The radiometric calibration establishes a relationship between the conditioned detector signal S' in units of DN and top-of-atmosphere spectral radiance L^{TOA}. S' is the detector signal after dark signal correction, linearity correction, gain matching and stray light correction.

$$R = \frac{L^{TOA}}{S'} \tag{1}$$

One radiometric coefficient is determined for each spectral channel. With this definition, radiometric coefficients depend on the integration time. In these proceedings, radiometric coefficients a reported for an integration time of 3.295 ms and 3.760 ms for VNIR and SWIR, respectively. Radiometric coefficients need to be scale appropriately for comparison with in-orbit data. The variation of the radiometric response within each spectral channel is described by the response non-uniformity (RNU) and does not depend on integration time.

4.2 Radiometric Coefficients

Radiometric Coefficients were determined by placing a 1.6 m diameter integrating sphere in front of the instrument to provide a homogeneous full-aperture illumination of the FOV with a known spectral radiance [8]. QTH lamps in the sphere provide a broadband spectrum covering the full spectral range of EnMAP. Lamps can be switched off individually to adjust the spectral radiance level. Traceability to national standards was established using a transfer spectrometer and an intermediate radiometric standard (RASTA) provided by DLR-IMF [9]. This intermediate standard can be traced to the National Metrology Institute of Germany (PTB).

Radiometric calibration was performed in air. Due to the air to vacuum shift discussed in Sec. 2, radiometric coefficients determined on ground are not directly applicable to in-orbit data. Using the known air-to-vacuum shift, however, radiometric calibration coefficients can be predicted for vacuum. To this end, the air pressure was monitored during the calibration to calculate for corrections.

Figure 21 shows radiometric coefficients derived during the on-ground calibration in air. The measurement uncertainty (k=2) including the uncertainty of the RASTA standard is < 2% (VNIR) and < 3.5% (SWIR).

(a) VNIR

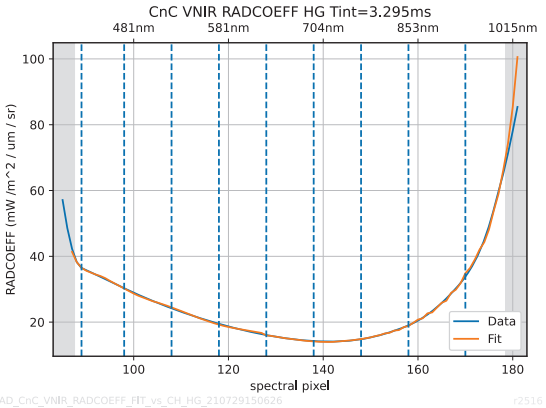

(b) SWIR

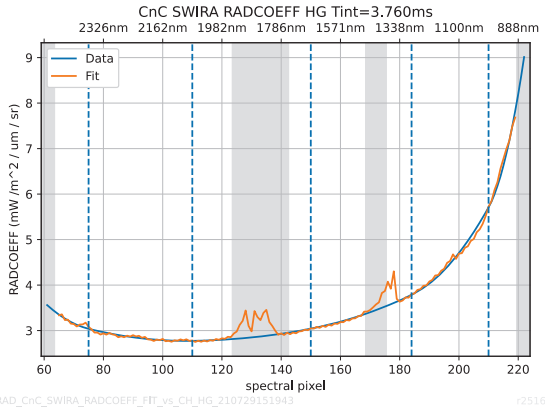

Figure 21 Radiometric coefficients determined in air at a pressure of 950mbar for VNIR (a) and SWIR (a). A smoothing spline is fitted to the data in order to obtain a smooth calibration curve which can be used to predict in-orbit performance. In the SWIR spectral region, spectral absorption features are clearly visible. They are excluded from the fitting process.

4.3 Response Non-Uniformity

Figure 22 shows Response Non-Uniformity (RNU) for a selected number of spectral channels before correction. After RNU correction, the non-uniformity is much improved.

(a) VNIR

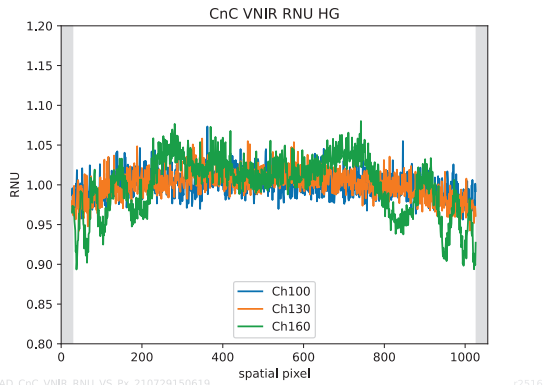

(b) SWIR

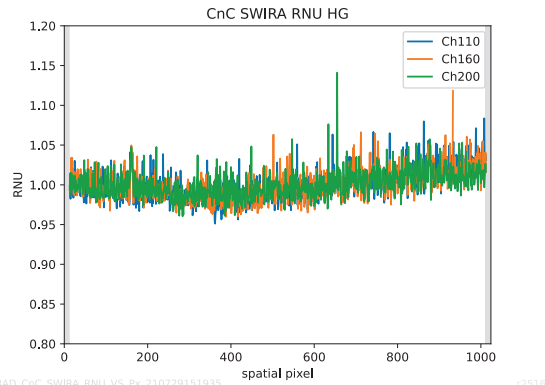

Figure 22 Response Non-Uniformity for VNIR (a) and SWIR (b) as a function of spatial pixel for three different spectral channels. The high spatial frequency structure arises from the pixel to pixel variation of radiometric response and is not due to measurement noise. For the VNIR spectrometer, fringing due to the etaloning effect in the detector is clearly visible.

4.4 Saturation

Figure 23 shows saturation levels of the EnMAP sensor for all spectral channels for the given integration time. Saturation levels are derived from detector Linear Full Well Capacity which is defined as the signal level at which the uncorrected signal vs irradiance curve deviates by more than 2% for a linear fit line. Saturation levels are determined independently for low gain and high gain.

(a) VNIR (b) SWIR

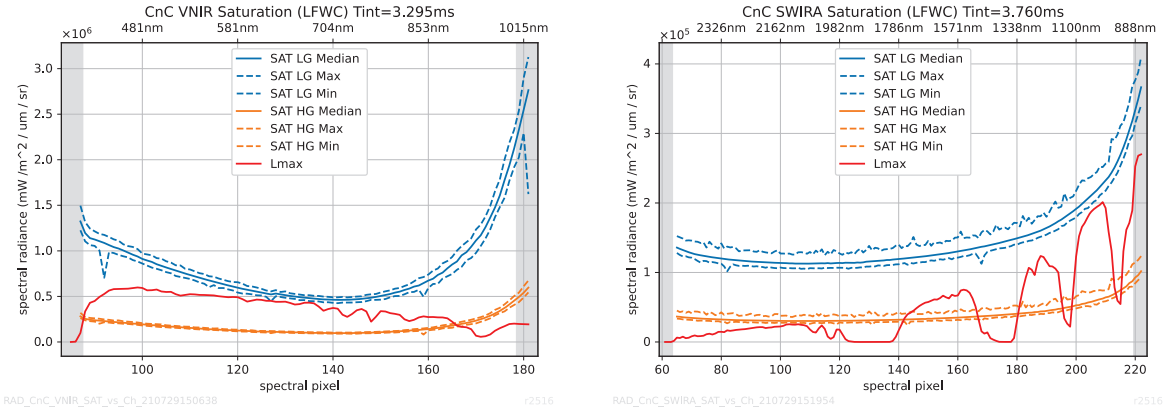

Figure 23 Saturation radiance as a function of spectral channel for VNIR (a) and SWIR (b). The saturation radiances shown for low gain (blue) and high gain (orange). The pixel-to-pixel distribution is captured by the median (solid lines) and maximum/minimum values (dashed lines). The maximum specified spectral radiance (90% reflectance, 0° sun incidence angle, 40 km visibility, target at sea level, rural aerosol, water vapor column 2 cm)

4.5 Signal-to-Noise Ratio

Signal-to-Noise Ratio was determined by illuminating the instrument at 14 radiance levels and recording 16384 frames per illumination level and gain setting. This allows to determine SNR as a function of detector signal in units of DN for each pixel. Figure 24 and Figure 25 aggregates the SNR measurements for VNIR and SWIR, respectively by binning the data of all pixels and calculating the median value as well as the 5st and 95th percentile. The measurement relative uncertainty (k=1) is 2.27% (VNIR) and 1.12% (SWIR) evaluated at an SNR of 500 and 150, respectively.

(a) Low Gain (b) High Gain

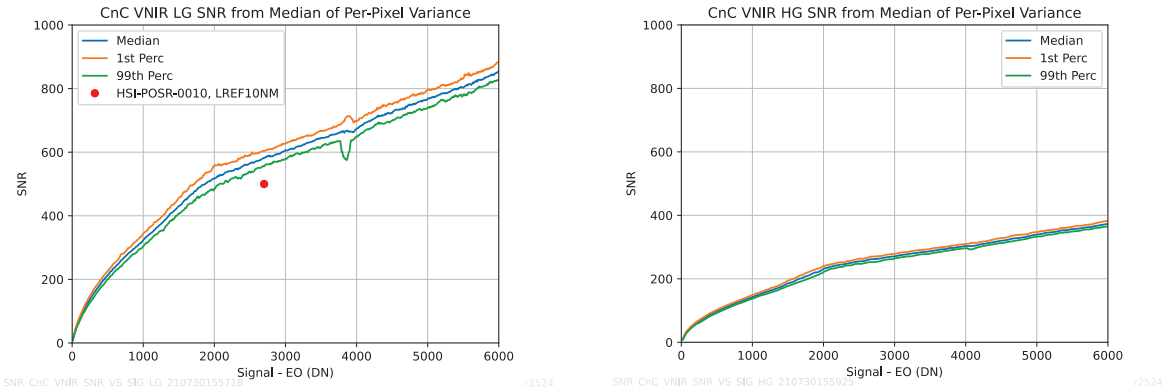

Figure 24 Signal-to-Noise ratio for VNIR as a function of signal after subtraction of the electronic offset for low gain (a) and high gain (b). SNR was determined for each pixel individually. The graphs shows the median of the distribution as well as 5% and 95% percentiles. The complex internal pixel structure of the VNIR detector results in a noise characteristic which cannot be described by a combination of signal independent electronic noise and shot noise.

(a) Low Gain (b) High Gain

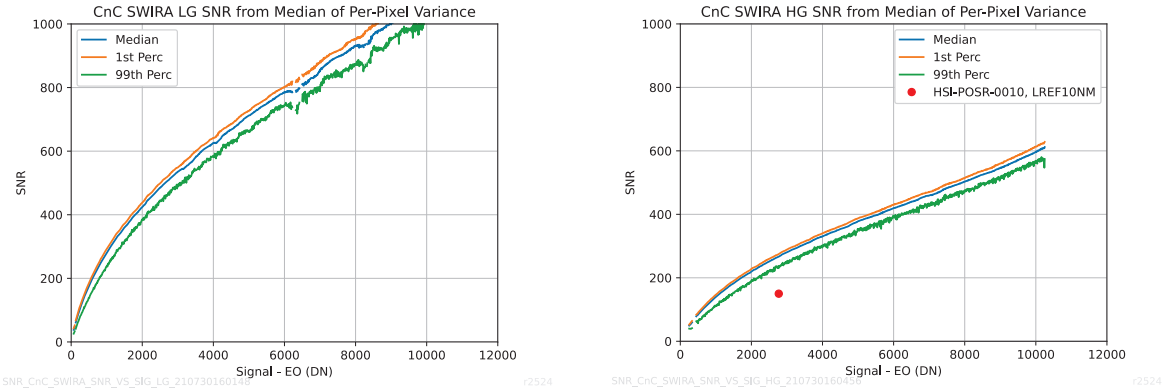

Figure 25 Signal-to-Noise ratio for SWIR as a function of signal after subtraction of the electronic offset for low gain (a) and high gain (b). SNR was determined for each pixel individually. The graphs shows the median of the distribution as well as 5% and 95% percentiles. The noise characteristic can well be described by a combination of signal independent electronic noise contribution and signal dependent shot noise.

The characterizations of the SNR performance can be used to predict radiometric sensitivity in terms of noise equivalent delta radiance (NEdL) for a reference spectrum L_{ref} (30% reflectance, 30° sun incidence angle, 40 km visibility, target at sea level, rural aerosol, water vapor column 2cm). To take into account the non-constant spectral resolution and spectral sampling distance, NEdL is normalized to a constant bandwidth of 10nm. Results are shown in Figure 26 for VNIR and in Figure 27 for SWIR. High values of NEdL are related to low radiometric response as shown in Figure 21. NEdL for a given reference spectrum depends on the integration time chosen and was evaluated for the same integration time as used for the radiometric coefficients.

(a) Low Gain (b) High Gain

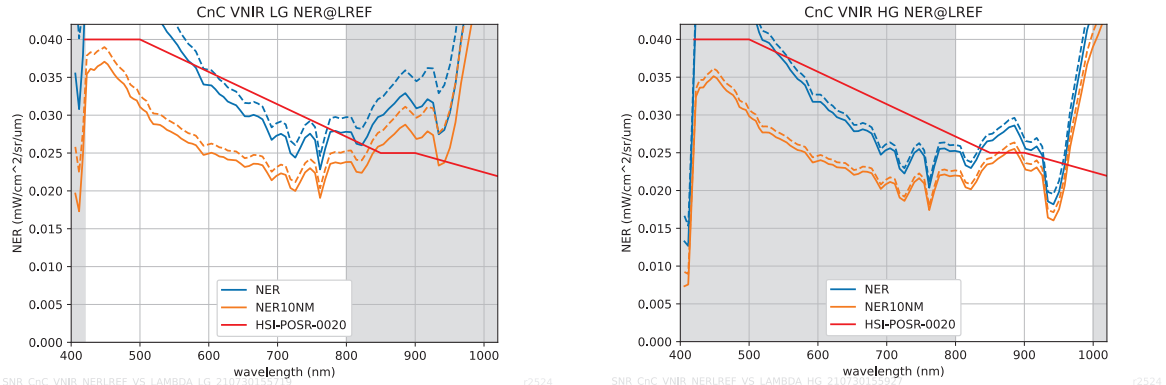

Figure 26 VNIR NEdL for low gain (a) and high gain (b) evaluated for the reference spectrum L_{ref}. NEdL is shown for the native spectral bandwidth (blue) and normalized to a bandwidth of 10nm (orange). Solid lines show the median of all pixels and dashed lines the 5% SNR percentile. During earth observation, the VNIR detector is operated auto-gain mode. Spectral ranges where the respective gain mode is not active or which are not part of the EnMAP spectral range are shaded in grey. NEdL increases at both ends of the spectrum in accordance with the radiometric coefficients.

(a) Low Gain

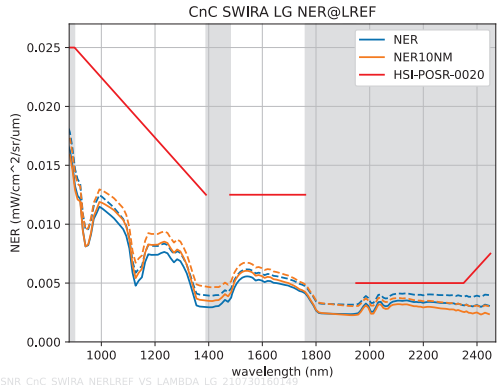

(b) High Gain

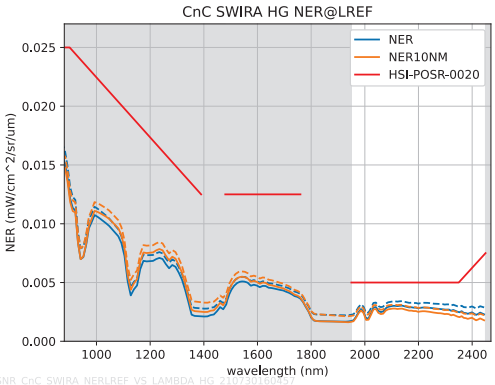

Figure 27 SWIR NEdL for low gain (a) and high gain (b) evaluated for the reference spectrum L_{ref}. NEdL is shown for the native spectral bandwidth (blue) and normalized to a bandwidth of 10nm (orange). Solid lines show the median of all pixels and dashed lines the 5% SNR percentile. During earth observation, the SWIR detector is operated in mixed gain modes where all above 1800 nm are operated in high gain and below 1800 nm in low gain. Spectral ranges where the respective gain mode is not active or which are not part of the EnMAP spectral range are shaded in grey.

5. POLARIMETRIC CHARACTERIZATION

For polarimetric characterization, the same setup was used as for the radiometric calibration [8]. A full aperture polarizer was placed between the integrating sphere and the instrument. The polarizer was rotated by 360° in steps of 20° and the detector signal of the instrument recorded for all pixels. The resulting measurement signal is shown in Figure 28. Fringes are visible due to the polarization sensitivity of the instrument. If the instrument was polarization insensitive a flat line would be observed. The polarization sensitivity is defined as the fringe visibility of the signal according to

$$POL_{i,j} = \frac{\max(S_{i,j}(\alpha)) - \min(S_{i,j}(\alpha))}{\max(S_{i,j}(\alpha)) + \min(S_{i,j}(\alpha))} \quad (2)$$

Here, α is the polarizer angle and S is the detector signal after dark signal subtraction for each pixel. The resulting polarization sensitivity of the instrument is shown in Figure 29. The overall polarization sensitivity agrees very well with predictions based polarization sensitive reflectivity measurements of mirror coatings. The absolute measurement uncertainty (k=2) is 0.0019.

(a) VNIR

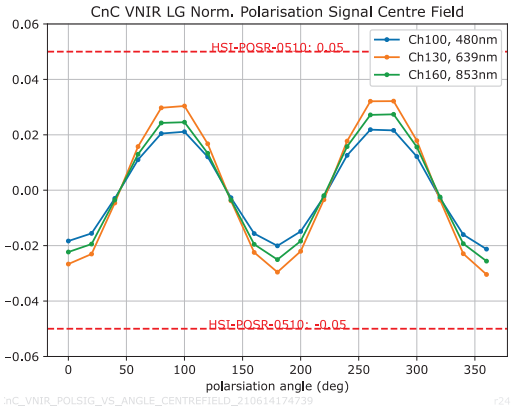

(b) SWIR

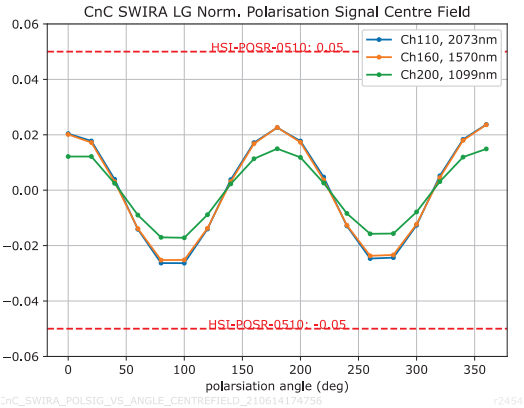

Figure 28 Polarization signal at the center of the VNIR (a) and SWIR (b) detector for three spectral channels. Shown is the deviation of the signal from the mean signal as a function of polarizer angle. The polarizer is rotated by 360° resulting in two fringes because the polarization produced by the polarizer is the same after a rotation of 180°.

(a) VNIR

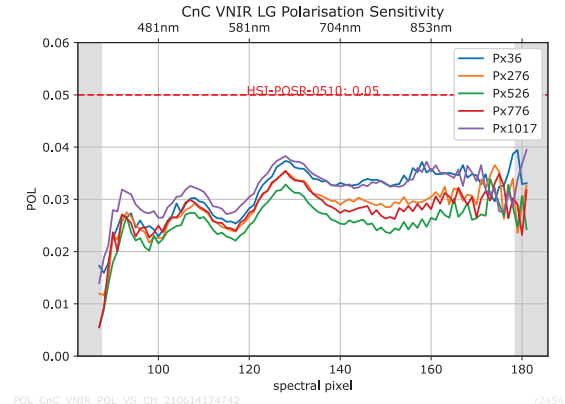

(b) SWIR

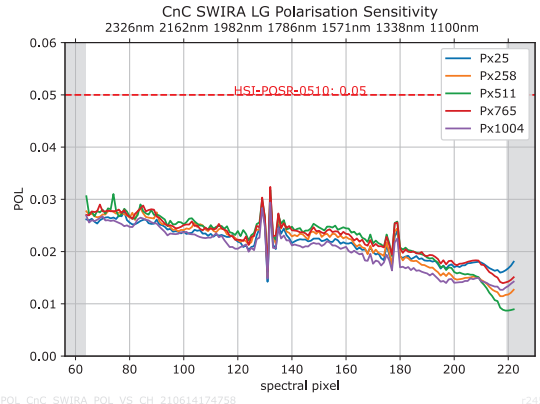

Figure 29 Polarization sensitivity as a function of spectral channel for 5 field positions for VNIR (a) and SWIR (b).

6. SUMMARY

In summary, the EnMAP instrument has been successfully characterized and calibrated on ground. The measurement uncertainties exceed what is required to generate valid calibration tables and verify performance requirements. This also shows that the bespoke OGSE developed specifically for the EnMAP project performed as expected.

The performance of the instrument is for the vast majority of performance parameters as expected from performance simulation. All deviation from predictions made during the design phase are well understood and explained. This includes the reduction of along-track FOV with wavelength, the reduced MTF of the VNIR spectrometers at long wavelengths, fringing due to VNIR detector etaloning and increased keystone for the SWIR spectrometer.

The characterization approach of performing measurements in air rather than in vacuum appears to be successful. In particular, shifts in the spectral calibration due to changes in air pressure can be corrected very well by accurately measuring the air pressure and using a correction model.

The results of the C&C campaign are in agreement with the end-to-end characterizations of the instrument which was conducted before the final integration of the HSI and the mating with the platform. The demonstrated stability of the instrument throughout the extensive testing it underwent on-ground promises excellent performance in-orbit.

ACKNOWLEDGEMENTS

The work presented herein was performed on behalf of the German Space Agency DLR with funds of the German Federal Ministry of Economic Affairs and Technology under the grant No. 50 EP 0801.

We would like to thank A. Baumgartner et al. (DLR-IMF) for support during the radiometric calibration of the instrument.

REFERENCES

[1] Guanter, L., Kaufmann, H., Segl, K., Foerster, S., Rogass, C., Chabrillat, S., Kuester, T., Hollstein, A., Rossner, G., Chlebek, C., Straif, C., Fischer, S., Schrader, S., Storch, T., Heiden, U., Mueller, A., Bachmann, M., Mühle, H., Müller, R., Habermeyer, M., Ohndorf, A., Hill, J., Buddenbaum, H., Hostert, P., van der Linden, S., Leitão, P., Rabe, A., Doerffer, R., Krasemann, H., Xi, H., Mauser, W., Hank, T., Locherer, M., Rast, M., Staenz, K., Sang, B., "The EnMAP Spaceborne Imaging Spectroscopy Mission for Earth Observation.," Remote Sensing 2015 7, 8830-8857 (2015). DOI: 10.3390/rs70708830.

[2] Wilkens, L., et al., "An On-Board Calibration Assembly (OBCA) on the EnMAP satellite," Proc. SPIE 10562, 1056244 (2016). DOI: 10.1117/12.2296123.

[3] Lettner, M., et al., "Versatile full aperture illumination OGSE setup for alignment and end-to-end calibration of the EnMAP HSI," Proc. SPIE 11180, 111806D (2018). DOI: 10.1117/12.2536148

[4] Pope, C. and Baumgartner, A., "Light source for stray light characterization of EnMAP spectrometers," Proc. SPIE 11151, 1115175 (2019)

[5] Schwarzmaier, T., Baumgartner, A., Gege, P., Kohler, C., and Lenhard, K., "The radiance standard RASTA of DLR's calibration facility for airborne imaging spectrometers," Proc. SPIE 8533, 85331U-85331U-6 (2012).

[6] Mücke, M., Sang, B., Heider, B., Honold, H.-P., Sorning, M., Fischer, S., "EnMAP – Hyperspectral Imager (HSI) for Earth Observation: Current Status," Proc. SPIE 11180, 1118067 (2018). DOI: 10.1117/12.2536142

[7] Baur, S., Wachter., R., Basili, P., Lettner, M., Mücke, M., Sornig, M., Fischer, S., Proc. SPIE 11151, Sensors, Systems, and Next-Generation Satellites XXIII, 111511B (10 October 2019); doi: 10.1117/12.2532715

[8] Leonhard Polz, Anna Serdyuchenko, M. Lettner, M. Mücke, S. Fischer, "Setups for alignment and on-ground calibration and characterization of the EnMAP hyperspectral imager," Proc. SPIE 11852, International Conference on Space Optics — ICSO 2020, 118526B (11 June 2021); doi:10.1117/12.2600240

[9] A. Baumgartner, and T. Schwarzmaier, [Traceable Radiometric Calibration of the German Imaging Spectrometer Satellite Mission EnMAP], (2017).